University of Wollongong
Research Online

Australian Institute for Innovative Materials - Papers

Australian Institute for Innovative Materials

1-1-2015

One-pot synthesis of ultra-small magnetite nanoparticles on the surface of reduced graphene oxide nanosheets as anodes for sodium-ion batteries

Shaohua Zhang
University of Wollongong, sz826@uowmail.edu.au

Weijie Li
University of Wollongong, wl347@uowmail.edu.au

Bien Tan
Huazhong University of Science and Technology

Shulei Chou
University of Wollongong, shulei@uow.edu.au

Zhen Li
University of Wollongong, zhenl@uow.edu.au

See next page for additional authors

Follow this and additional works at: https://ro.uow.edu.au/aiimpapers

 Part of the Engineering Commons, and the Physical Sciences and Mathematics Commons

Recommended Citation

Zhang, Shaohua; Li, Weijie; Tan, Bien; Chou, Shulei; Li, Zhen; and Dou, S X., "One-pot synthesis of ultra-small magnetite nanoparticles on the surface of reduced graphene oxide nanosheets as anodes for sodium-ion batteries" (2015). *Australian Institute for Innovative Materials - Papers*. 1337.
https://ro.uow.edu.au/aiimpapers/1337

Research Online is the open access institutional repository for the University of Wollongong. For further information contact the UOW Library: research-pubs@uow.edu.au

One-pot synthesis of ultra-small magnetite nanoparticles on the surface of reduced graphene oxide nanosheets as anodes for sodium-ion batteries

Abstract

Nanocomposites with ultra-small magnetite (Fe_3O_4) nanoparticles (approx. 3 nm) uniformly anchored on the surfaces of reduced graphene oxide (RGO) nanosheets were successfully synthesized for anodes in sodium-ion batteries by a novel single-step high-temperature coprecipitation approach. The best electrode delivers a reversible Na^+ storage capacity of 204 mA h g^{-1} with excellent capacity retention, *i.e.*, 98% of the second-cycle value was retained after 200 cycles.

Keywords

magnetite, nanoparticles, surface, reduced, graphene, one, oxide, synthesis, nanosheets, anodes, sodium, ion, batteries, ultra, pot, small

Disciplines

Engineering | Physical Sciences and Mathematics

Publication Details

Zhang, S., Li, W., Tan, B., Chou, S., Li, Z. & Dou, S. (2015). One-pot synthesis of ultra-small magnetite nanoparticles on the surface of reduced graphene oxide nanosheets as anodes for sodium-ion batteries. Journal of Materials Chemistry A, 3 (9), 4793-4798.

Authors

Shaohua Zhang, Weijie Li, Bien Tan, Shulei Chou, Zhen Li, and S X. Dou

This journal article is available at Research Online: https://ro.uow.edu.au/aiimpapers/1337

Journal Name

COMMUNICATION

Cite this: DOI: 10.1039/x0xx00000x

One-pot synthesis of ultra-small magnetite nanoparticles on the surface of reduced graphene oxide nanosheets as anode for sodium-ion batteries

Received 00th January 2012,
Accepted 00th January 2012

DOI: 10.1039/x0xx00000x

www.rsc.org/

Shaohua Zhang,[a] Weijie Li,[a] Bien Tan,[c] Shulei Chou,[a] Zhen Li,[a,b,*] and Shixue Dou[a]

Nanocomposites with ultra-small magnetite (Fe_3O_4) nanoparticles (~3 nm) uniformly anchored on the surfaces of reduced graphene oxide (RGO) nanosheets have been successfully synthesized for anodes in sodium-ion batteries by a novel single-step high-temperature coprecipitation approach. The electrode delivers a reversible Na^+ storage capacity of 204 mAh g^{-1} with an excellent capacity retention, i.e., 98% of the second-cycle value was retained after 200 cycles.

Developing effective renewable energy sources to meet increasing energy demands has been an urgent issue. During the past several decades, lithium ion batteries (LIBs) have attracted considerable attention in both industrial and scientific fields due to their high energy density, fast charge/discharge rate, and durable cycling performance.[1-3] The high cost and limited nature of lithium resources, however, make LIBs unable to satisfy the requirements for large-scale energy storage.[4] To overcome this issue, great efforts have been made in recent years to develop low-cost and environmentally benign batteries, among which, sodium ion batteries (SIBs) are considered to be the most promising candidate for large-scale applications, owing to the huge abundance and low cost of sodium resources.[5-7] Nevertheless, there have not been many breakthroughs in the past few decades, because of the lack of suitable host materials that have sufficient storage capacity and cycling stability for the Na^+ insertion reaction.[8, 9] Recently, iron-based transition metal oxides have been applied as anode materials in LIBs, among which, Fe_3O_4 has been the subject of intensive study due to its low cost, large abundance, environmental benignity, and excellent theoretical capacity (~ 924 mA h g^{-1}) , which is much higher than that of commercial graphite anodes (~372 mA h g^{-1}).[10-14] Its performance is lacking, however, due to both large volume expansion/contraction during cycling and poor conductivity.

To solve the aforementioned problem, two strategies have been proposed, including reducing the particle size of the electrode materials and introducing a carbon matrix.[15-17] Small particles can shorten the diffusion paths of Na^+ ions, which is crucial for sodium storage because a Na^+ ion is about 55% larger than a Li^+ ion.[18] Therefore, ultra-small monodisperse Fe_3O_4 nanocrystals are expected to be excellent novel electrode materials. Moreover, anchoring the Fe_3O_4 nanoparticles onto a carbon matrix can effectively cushion the volume expansion/contraction and improve their electronic conductivity. Two-dimensional graphene has been successfully used as such a matrix owing to its excellent conductivity, high surface area, and superior mechanical flexibility.[19, 20] Therefore, nanocomposites from ultra-small Fe_3O_4 nanocrystals and graphene nanosheets are expected to be excellent electrodes for SIBs. There are some reports on the application of Fe_3O_4 nanoparticles in SIBs,[21-24] but no report on graphene/ultra-small Fe_3O_4 nanocomposites as anodes in SIBs.

Herein, we report a novel and facile one-pot approach to the synthesis of RGO/Fe_3O_4/PMAA-PTMP nanocomposites (referred to RGOF) as high-performance anodes for SIBs (Scheme 1), directly

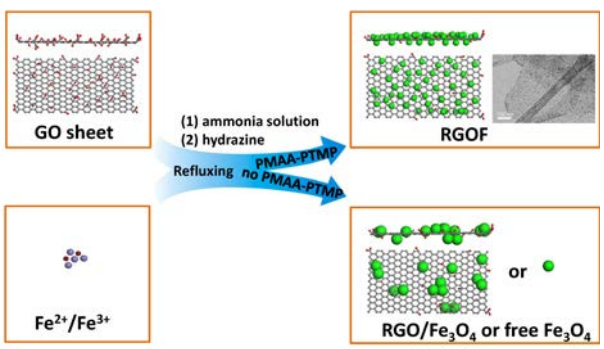

Scheme 1. Schematic illustration of the synthesis of Fe_3O_4 and RGO composites.

from graphene oxide (GO) nanosheets, thiolfunctionalized poly (methacrylic acid), (PMAA-PTMP, shown by Scheme S1 in the Supporting Information,), and an iron precursor (Fe^{2+}, Fe^{3+}) solution. PMAA-PTMP was used as a capping agent[25-30] to protect the ultra-small Fe_3O_4 nanoparticles from coagulation to ensure that they are evenly anchored on the RGO nanosheets. Three composites were synthesized with a volume of GO of 0.5 mL (~2.67 mg GO), 1 mL (~5.34 mg GO) and 1.5 mL (~8.01 mg GO), and are denoted as RGOF-1, RGOF-2, and RGOF-3, respectively. For comparison, bare RGO/Fe_3O_4 nanocomposite without PMMA-PTMP and

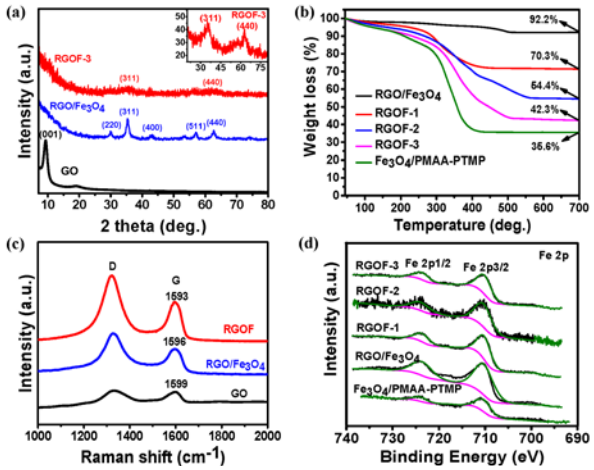

Figure 1. (a) XRD patterns of GO, RGO/Fe_3O_4, and RGOF-3 nanocomposite, inset: enlargement of XRD pattern of RGOF-3 for the indicated range. (b) TGA curves for Fe_3O_4/PMMA-PTMP, RGO/Fe_3O_4, and RGOF composites in air. (c) Raman spectra of GO, Fe_3O_4/RGO, and RGOF. (d) XPS spectra of Fe 2p for pristine Fe_3O_4, Fe_3O_4/RGO, and the RGOF

Fe_3O_4/PMMA-PTMP without RGO nanosheets were also synthesized using the same procedure. The results show that the RGOF nanocomposites feature large reversible capacity, and excellent cycling performance and rate capability because of the uniform distribution of ultra-small Fe_3O_4 nanoparticles (~3 nm) and the buffering role of the RGO nanosheets.

The crystal structures of the GO, RGO/Fe_3O_4, and RGOF nanocomposites were determined by X-ray diffraction (XRD), as shown in Figure 1(a) and Figure S1. The XRD pattern of GO shows a strong peak at $2\theta = 9.3^\circ$, indicating the successful formation of GO nanosheets with oxygen-containing functional groups through the oxidation of graphite.[31] Unlike the GO nanosheets, the RGOF nanocomposites have no peak at 9.3° in their XRD patterns, suggesting the absence of stacked RGO nanosheets in these composites.[31] All diffraction peaks of Fe_3O_4 in the RGO/Fe_3O_4 nanocomposites match well with cubic magnetite (JCPDS: 65-3107, a=8.391 Å) without any impurity. A typical pattern of RGOF is shown in Figure 1(a), and the enlarged peaks in the inset are broadened due to the ultra-small size of the Fe_3O_4 nanoparticles. Figure 1(b) displays the mass loss of Fe_3O_4/PMMA-PTMP, RGO/Fe_3O_4, and the RGOF nanocomposites, as determined by thermogravimetric analysis (TGA) measurements in air, which indicate that the contents of Fe_3O_4 in the Fe_3O_4/PMMA-PTMP, RGO/Fe_3O_4, RGOF-1, RGOF-2 and RGOF-3 are about 35.6wt%, 92.2wt%, 70.3wt%, 54.4wt%, and 42.3wt%, respectively. According to the weight changes of RGO/Fe_3O_4, RGOF-1, RGOF-2, RGOF-3 under the argon atmosphere in Figure S2, the contents of RGO in RGO/Fe_3O_4, RGOF-1, RGOF-2, RGOF-3 are estimated to be about 1.8 wt%, 2.0 wt%, 8.1 wt%, 17.8 wt%, respectively.

The Raman spectra in Figure 1(c) show the typical D-band (~1332 cm^{-1}) and G-band (~1599 cm^{-1}) of GO, Fe_3O_4/RGO, and the RGOF nanocomposites.[32] The D band is caused by structural defects or edges in graphene, and the G band corresponds to the first-order scattering of the E_{2g} mode observed for sp^2 carbon domains. The intensity ratio of the D band to the G band (I_D/I_G) acts as a ruler to measure the degree of graphitization of carbon materials. The I_D/I_G ratio increases from 1.03 for GO nanosheets to 1.49 and 1.59 for RGO/Fe_3O_4 and the RGOF nanocomposites, respectively, indicating increased disorder of the graphene layers in the composites.[2, 32] It was reported that the shift in the G band of carbon-based composites

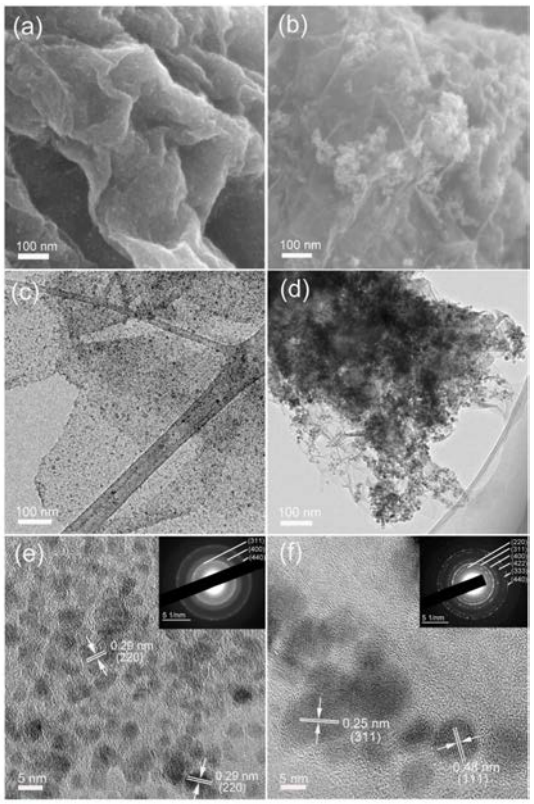

Figure 2. FESEM and TEM images of as-prepared RGOF-3 (a, c, e) and RGO/Fe_3O_4 (b, d, f) nanocomposites. The insets in (e) and (f) show the corresponding SAED patterns.

with nanocrystals means that there is charge transfer between the carbon and the nanocrystals.[33, 34] The blue-shift of the G band from 1599 cm^{-1} (GO) to 1593 cm^{-1} (RGOF) and 1596 cm^{-1} (RGO/Fe_3O_4) may indicate more charge transfer from graphene to Fe_3O_4 in RGOF than in RGO/ Fe_3O_4. Figure S3 shows the Fourier transform infrared (FT-IR) transmittance of pure PMAA-PTMP, Fe_3O_4/PMMA-PTMP, GO, RGO/Fe_3O_4, and the RGOF nanocomposites. The spectra of PMAA-PTMP and GO exhibit the characteristic peaks at 3156, 1735, and 1224 cm^{-1} from the stretching of the O-H, C=O, and C-O bonds, respectively. Compared with GO, RGO/Fe_3O_4 and RGOF have two new peaks at 1575 and 576 cm^{-1}, which are attributed to the coordination of surface iron ions of Fe_3O_4 and carboxylic groups in the RGO sheets, and the Fe-O bond in the crystalline lattice of Fe_3O_4.[35-39] In addition, the absence of peak at 1735 cm^{-1} and a decrease in the intensity of the broad band at 3156 cm^{-1} in the spectrum of RGO/Fe_3O_4 composite compared to that of GO supports the reduction of functional groups by hydrazine, which is consistent with the XRD and Raman results. X-ray photoelectron spectroscopy (XPS) spectra [Figure 1(d) and Figure S4] demonstrate the presence of Fe, O, and C in the RGOF composites. Oxygenated carbon is significantly decreased in RGOF-3 [Fig. S4(c)] in comparison with the GO nanosheets [Fig. S4(b)], suggesting the successful reduction of GO. Figure 1(d) presents the typical peaks of Fe $2p_{3/2}$ and Fe $2p_{1/2}$ at 711.6 and 724.5 eV, respectively, from the Fe_3O_4 nanoparticles. The absence of the characteristic satellite peak of Fe_2O_3 around 719.2 eV[40-42] confirms the formation of the Fe_3O_4.

The morphology and microstructure of these samples were characterized by field emission scanning electron microscopy (FESEM) and transmission electron microscopy (TEM) (Figure 2

and Figures S5-S7). The SEM image of RGOF-3 in Figure 2(a) shows the wrinkled RGO nanosheets and ultra-small Fe_3O_4 nanoparticles, which are evenly anchored on the surfaces of the RGO sheets, which can be further clearly observed in Figure 2(c, e) and Figure S4. It is evident that RGO nanosheets are well decorated by a large quantity of ultra-small Fe_3O_4 nanoparticles with an average size of 3 nm (Figure S5). The well-defined crystalline lattice can be identified, with *d*-spacings of 0.48 nm, 0.29 nm, and 0.25 nm, corresponding to the (111), (220), and (311) planes of with a pore volume of 0.158, 0.608, 0.264 and 0.124 cm^3g^{-1} respectively (Figure S9 and Table S1 in the Supporting Information).

The electrochemical performances of Fe_3O_4/PMMA-PTMP, RGO/Fe_3O_4, and the RGOF nanocomposites were tested with a view to their use as anodes for sodium ion batteries in the voltage range of 0-2 V in an electrolyte consisting of 1.0 mol/L $NaClO_4$ in a mixture of ethylene carbonate (EC) - diethyl carbonate (DEC) solution (1:1 v/v), with 5 vol.% addition of fluoroethylene carbonate (FEC).[43] Fig. 3(a-c) presents the charge-discharge curves of the

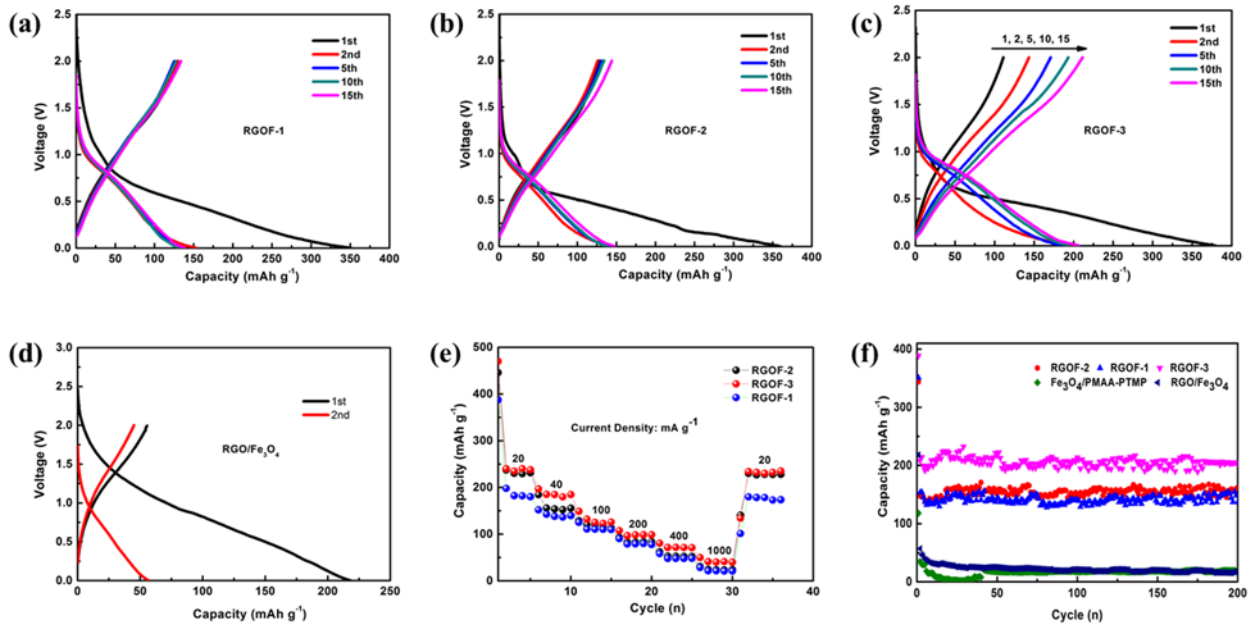

Figure 3. Electrochemical performance of the nanocomposites. (a-d) the charge-discharge curves for selected cycles of RGOF-1, RGOF-2, RGOF-3, and RGO/Fe_3O_4, respectively; (e) rate capability of the RGOF composites; (f) cycling performance of RGOF compared with RGO/Fe_3O_4 and Fe_3O_4/PMMA-PTMP.

Fe_3O_4, which also can be further confirmed by the selected area electron diffraction (SAED) pattern shown in Figure 2(e). These ultra-small Fe_3O_4 nanoparticles are densely and evenly dispersed on both sides of the sheets [Figure 2 (a, c, e) and Figure S8], and there is no unoccupied RGO nanosheets. It should be noted that no aggregates of Fe_3O_4 nanoparticles were observed on the RGO nanosheets, although their share of mass in the composites is up to 60%. In contrast, in the RGO/Fe_3O_4 composite prepared in the absence of PMAA-PTMP, the spherical Fe_3O_4 nanoparticles have quite a large size [(12.2 ± 1.6) nm], and they easily aggregate into clusters, as shown in Figure 2(b, d) and Figure S6]. In addition, many free Fe_3O_4 nanoparticles without RGO sheets are found in the composites [Figure S6(c)]. These results highlight the important role of PMAA-PTMP in preventing aggregation of nanoparticles. In the three RGOF nanocomposites, the Fe_3O_4 nanoparticles become smaller and more uniform [i.e. from (5.79 ± 1.6) nm through (3.73 ± 0.6) nm to (3.06 ± 0.6) nm] as the amount of GO increases from 0.5 mL, through 1.0 mL to 1.5 mL, as shown in Figure S7. This could arise from the strong electrostatic interactions between the positive Fe^{2+}/Fe^{3+} ions and the negative carboxyl and hydroxyl groups on the surfaces of the GO nanosheets. More GO nanosheets provide more functional groups and a larger area for the nucleation and growth of ultra-small Fe_3O_4 nanoparticles. The Brunauer-Emmett-Teller (BET) specific surface area of the Fe_3O_4/PMMA-PTMP, RGO/Fe_3O_4, RGOF-1 and RGOF-3 are 177.76, 147.67, 167.92 and 137.34 m^2g^{-1}

electrodes containing RGOF nanocomposites at a current density of 40 mA g^{-1}. The RGOF-1 delivered an initial discharge capacity of 350 mAh g^{-1}, with a coulombic efficiency of ~ 40 %.The close overlapping of all the discharge curves after 2 cycles suggests the excellent cycling performance of the electrode. The discharge capacity of RGOF-1 composite remained ~150 mAh g^{-1}, with a coulombic efficiency of ~90% [Figure 3(a)]. The low initial coulombic efficiency is a common phenomenon for transition metal oxide based anodes for LIBs and SIBs.[44] Similarly, the RGOF-2 electrode delivered an initial discharge capacity of 360 mAh g^{-1} and remained at 150 mAh g^{-1} after the second cycle. The RGOF-3 composite with more RGO content shows a larger capacity than the other two composites, delivering 380 and 204 mAh g^{-1} for the initial and stable capacity, respectively. The capacity of the RGO/Fe_3O_4 electrode, however, in Figure 3(d) decreases from the initial discharge capacity of 218 mAh g^{-1} to only 57 mAh g^{-1} at the second cycle. Compared with Fe_3O_4/PMMA-PTMP nanoparticles, the introduction of RGO nanosheets significantly improves the electrical conductivity (Figure S10 in the Supporting Information).

For composites based electrodes, their capacities include contributions from each component. The capacities of our electrodes would consist of contributions from Fe_3O_4 nanoparticles and RGO nanosheets, if the other contributions are negligible. Table 1 summarizes the mass of electrodes, the capacity, and standardized capacity by Fe_3O_4 in each electrode. The size of Fe_3O_4 nanoparticles and their weight percentage in active materials determined by TGA

is also displayed in Table 1. The calculation of standardized capacity is based on the reversible capacity of RGO is 174.3 mAh g^{-1} at 40 mA g^{-1}.[45] It clearly shows that the standardized capacity notably increases with the decrease of particle size, which supports the smaller particle size, the better performance.

Table 1. The particle size of Fe_3O_4, the mass of active materials, percentages of Fe_3O_4 and RGO, overall capacity and standardized capacity of each electrode.

Sample	Size (nm)	Mass of electrode (mg)^{Me}	Weight percentage of Fe_3O_4 (%)^{WF}	Weight percentage of RGO (%)^{WR}	Fe_3O_4 (mg)^{MF}	RGO (mg)^{MR}	Capacity (mAh g^{-1})^{Ce}	Standardized capacity of Fe_3O_4 (mAh g^{-1}) ^{SF}
RGOF-1	5.79	1.98	70.3	2	1.3919	0.0396	136.9	189.778
RGOF-2	3.73	2.05	54.4	8.1	1.1152	0.16605	162.1	272.025
RGOF-3	3.06	1.92	42.3	17.8	0.8121	0.34176	204	408.923
RGO/Fe_3O_4	12.2	2.12	92.2	1.8	1.9546	0.03816	17.6	15.686
Fe_3O_4/PMAA-PTMP	4.5*	1.89	35.6	0	0.6728	0	19	53.370

SF=(Ce×Me-174.3 mA h g^{-1}×MR)÷MF

The rate capability of the RGOF based electrodes were investigated at a variety of current densities between 20 mA g^{-1} and 1000 mA g^{-1}, as presented in Figure 3(e) and Figure S11. Clearly, the electrode containing RGOF-3 has the best rate capability in comparison with the electrodes made from the other two RGOF composites. In Figure 3(e), the average capacity for the first 5 cycles for RGOF-3 obtained with a current density of 20 mA g^{-1} is 246 mAh g^{-1}. Increasing the current density to 40 mA g^{-1}, 100 mA g^{-1}, and 1000 mA g^{-1} leads to a decrease in the five-cycle average capacity, i.e. from 246 mAh g^{-1} to 42 mAh g^{-1}. The half cells still retained ~17 % of initial capacity, even when the current density was as high as 1000 mA g^{-1}. The charge-discharge curves of RGOF based electrodes demonstrate that the potential polarization increases with the increase in current density (Figure S11). Figure 3(f) shows the cycling performance of the RGOF based electrodes compared with those made from RGO/Fe_3O_4 and Fe_3O_4/PMMA-PTMP at a current density of 40 mA g^{-1}. It clearly shows that the cycling performance of the electrodes made from the RGOF nanocomposites is much better than those made from Fe_3O_4/PMMA-PTMP and RGO/Fe_3O_4. The capacities slightly increase during cycling due to the increase in the spacing of graphene oxide layers arising from continuous insertion/extraction of Na ions. The capacity of the Fe_3O_4/PMMA-PTMP electrode drastically decreased to a capacity of 40 mAh g^{-1} after 5 cycles. After 200 cycles, the RGOF-3 electrode, on the other hand, retained 98% capacity with respect to the second cycle (208 mAh g^{-1}). This electrode exhibits the highest capacity and rate capability among all the RGOF electrodes.

The excellent electrochemical performance of the RGOF electrodes can be attributed to the following three factors: (1) RGO nanosheets afford not only a superior electrically conductive matrix for the composite, but also an elastic buffer to mitigate cracking of the Fe_3O_4 nanoparticles associated with expansion and contraction during the uptake and release of Na^+ ions. (2) RGO nanosheets and ultra-small Fe_3O_4 nanoparticles effectively shorten the diffusion length of Na^+ ions. (3) The unique structure of the RGOF composites has benefits for performance because monodisperse Fe_3O_4 nanoparticles grew evenly *in-situ* on the surfaces of the RGO nanosheets, so that they avoided aggregates, which could be destroyed during charge and discharge.

Conclusions

In summary, we have synthesized unique RGOF nanocomposites consisting of ultra-small Fe_3O_4 and RGO nanosheets in the presence of PMAA-PTMP through a novel single-step high-temperature coprecipitation approach. The resultant RGOF nanocomposites have been investigated as anode material for SIBs. The electrodes show superior cycling performance with a reversible Na-storage capacity of 204 mAh g^{-1} and outstanding cycling stability (i.e. 98% capacity was retained after 200 cycles). The excellent electrochemical performance can be attributed to the synergetic effect of monodisperse ultra-small Fe_3O_4 nanoparticles and highly conductive RGO nanosheets. These advantages, together, with their low cost and environmental friendliness, make these nanocomposites a promising anode candidate for sodium-ion batteries.

Acknowledgements

S. Zhang gratefully acknowledges the Chinese Scholarship Council (CSC) for his scholarship. Z. Li acknowledges support from the Australian Research Council (ARC) through the Discovery Projects DP130102699 and DP130102274. S. Dou is grateful for support from the Baosteel-Australia Research Centre (BARC) through the project BA110011 and from the ARC through the Linkage Project LP120200289. The authors also appreciate support from Institute of Superconducting & Electronic Materials (ISEM) and the Electron Microscopy Centre (EMC) at UOW, and also thank Dr. Tania Silver for critical reading of the manuscript.

Notes and references

[a] Institute for Superconducting and Electronic Materials, Australian Institute for Innovative Materials, University of Wollongong, Squires Way, North Wollongong, NSW 2500, Australia. E-mail: zhenl@uow.edu.au; Fax: +61-2-42215731; Tel: +61-2-42215163

[b] School of Radiation Medicine and Radiation Protection, Collaborative Innovation Center of Radiological Medicine of Jiangsu Higher Education Institutions, Soochow University, 199 RenAi Road, Suzhou Industrial Park, Suzhou 215123, China.

[c] School of Chemistry and Chemical Engineering, Huazhong University of Science and Technology, Wuhan 430074, China.

Electronic Supplementary Information (ESI) available: [details of any supplementary information available should be included here]. See DOI: 10.1039/c000000x/

1 J. M. Tarascon, M. Armand, *Nature*, 2001, **414**, 359.

2 P. Poizot, S. Laruelle, S. Grugeon, L. Dupont, J. M. Tarascon, *Nature*, 2000, **407**, 496.

3 K. Kang, Y. S. Meng, J. Bréger, C. P. Grey, G. Ceder, *Science*, 2006, **311**, 977.

4 M. Armand, J. M. Tarascon, *Nature*, 2008, **451**, 652.

5 V. Palomares, P. Serras, I. Villaluenga, K. B. Hueso, J. Carretero-Gonzalez, T. Rojo, *Energy Environ. Sci.*, 2012, **5**, 5884.

6 S. Komaba, W. Murata, T. Ishikawa, N. Yabuuchi, T. Ozeki, T. Nakayama, A. Ogata, K. Gotoh, K. Fujiwara, *Adv. Funct. Mater.*, 2011, **21**, 3859.

7 R. Alcántara, M. Jaraba, P. Lavela, J. L. Tirado, *Chem. Mater.*, 2002, **14**, 2847.

8 C. Delmas, J. J. Braconnier, C. Fouassier, P. Hagenmuller, *Solid State Ionics*, 1981, **3–4**, 165.

9 K. M. Abraham, *Solid State Ionics*, 1982, **7**, 199.

10 H. B. Wu, J. S. Chen, H. H. Hng, X. W. Lou, *Nanoscale*, **2012**, *4*, 2526.

11 B. Li, H. Cao, J. Shao, M. Qu, *Chem. Commun*, 2011, **47**, 10374.

12 S. K. Behera, *Chem. Commun.*, 2011, **47**, 10371.

13 G. Zhou, D. W. Wang, F. Li, L. Zhang, N. Li, Z. S. Wu, L. Wen, G. Q. Lu, H. M. Cheng, *Chem. Mater.*, 2010, **22**, 5306.

14 L. Ji, Z. Tan, T. R. Kuykendall, S. Aloni, S. Xun, E. Lin, V. Battaglia, Y. Zhang, *Phys. Chem. Chem. Phys*, 2011, **13**, 7170.

15 B. Qu, C. Ma, G. Ji, C. Xu, J. Xu, Y. S. Meng, T. Wang, J. Y. Lee, *Adv. Mater.*, 2014, **26**, 3854.

16 P. G. Bruce, B. Scrosati, J.-M. Tarascon, *Angew. Chem., Int. Ed.*, 2008, **47**, 2930.

17 W. Y. Li, L. N. Xu, J. Chen, *Adv. Funct. Mater.*, 2005, **15**, 851.

18 L. Fu, K. Tang, K. Song, P. A. van Aken, Y. Yu, J. Maier, *Nanoscale*, 2014, **6**, 1384.

19 Y. Zhu, S. Murali, M. D. Stoller, K. J. Ganesh, W. Cai, P. J. Ferreira, A. Pirkle, R. M. Wallace, K. A. Cychosz, M. Thommes, D. Su, E. A. Stach, R. S. Ruoff, *Science*, 2011, **332**, 1537.

20 K. S. Novoselov, A. K. Geim, S. V. Morozov, D. Jiang, M. I. Katsnelson, I. V. Grigorieva, S. V. Dubonos, A. A. Firsov, *Nature*, 2005, **438**, 197.

21 D.-Y. Park, S. T. Myung, *ACS Appl. Mater. Interfaces*, 2014, **6**, 11749.

22 S. M. Oh, S. T. Myung, C. S. Yoon, J. Lu, J. Hassoun, B. Scrosati, K. Amine, Y. K. Sun, *Nano Lett.*, 2014, **14**, 1620.

23 K. Shinichi, T. Mikumo, N. Yabuuchi, A. Ogata, H. Yoshida, Y. Yamadab, *J. Electrochem. Soc.*, 2010, **157**, A60.

24 S. Hariharan, K. Saravanan, V. Ramar, P. Balaya, *Phys. Chem. Chem. Phys.*, 2013, **15**, 2945.

25 X. Huang, Y. Luo, Z. Li, B. Li, H. Zhang, L. Li, I. Majeed, P. Zou, B. J. Tan, *Phys. Chem. C*, 2011, **115**, 16753.

26 H. Zhang, X. Huang, L. Li, G. Zhang, I. Hussain, Z. Li, B. Tan, *Chem. Commun.*, 2012, **48**, 567.

27 Z. Li, Q. Sun, Y. Zhu, B. Tan, Z. P. Xu, S. X. Dou, *J. Mater. Chem. B*, 2014, **2**, 2793.

28 Z. Li, S. X. Wang, Q. Sun, H. L. Zhao, H. Lei, M. B. Lan, Z. X. Cheng, X. L. Wang, S. X. Dou, G. Q. Lu, *Adv. Healthcare Mater.*, 2013, **2**, 958.

29 Z. Li, P. W. Yi, Q. Sun, H. Lei, H. L. Zhao, Z. H. Zhu, S. C. Smith, M. B. Lan, G. Q. Lu, *Adv. Funct. Mater.*, 2012, **22**, 2387.

30 Z. Li, B. Tan, M. Allix, A. I. Cooper, M. J. Rosseinsky, *Small*, 2008, **4**, 231.

31 D. C. Marcano, D. V. Kosynkin, J. M. Berlin, A. Sinitskii, Z. Sun, A. Slesarev, L. B. Alemany, W. Lu, J. M. Tour, *ACS Nano*, 2010, **4**, 4806.

32 S. Stankovich, D. A. Dikin, R. D. Piner, K. A. Kohlhaas, A. Kleinhammes, Y. Jia, Y. Wu, S. T. Nguyen, R. S. Ruoff, *Carbon*, 2007, **45**, 1558.

33 R. Kitaura, N. Imazu, K. Kobayashi, H. Shinohara, *Nano Lett.*, 2008, **8**, 693.

34 A. M. Rao, P. C. Eklund, S. Bandow, A. Thess, R. E. Smalley, *Nature*, 1997, **388**, 257.

35 B. Li, H. Cao, J. Shao, M. Qu, J. H. Warner, *J. Mater. Chem.*, 2011, **21**, 5069.

36 C. Nethravathi, M. Rajamathi, *Carbon*, 2008, **46**, 1994.

37 Z. Li, L. Wei, M. Y. Gao, H. Lei, *Adv. Mater.*, 2005, **17**, 1001.

38 Z. Li, Q. Sun, M. Gao, *Angew. Chem. Int. Ed.*, 2005, **44**, 123.

39 Z. Li, H. Chen, H. Bao, M. Gao, *Chem. Mater.*, 2004, **16**, 1391.

40 D. D. Hawn, B. M. DeKoven, *Surf. Interface Anal.*, 1987, **10**, 63.

41 X. Zhu, Y. Zhu, S. Murali, M. D. Stoller, R. S. Ruoff, *ACS Nano*, 2011, **5**, 3333.

42 T. Fujii, F. M. F. de Groot, G. A. Sawatzky, F. C. Voogt, T. Hibma, K. Okada, *Phys. Rev. B*, 1999, **59**, 3195.

43 C. Han, Z. Li, W. J. Li, S. L. Chou, S. X. Dou, *J. Mater. Chem. A*, 2014, **2**, 11683.

44 Z. Jian, B. Zhao, P. Liu, F. Li, M. Zheng, M. Chen, Y. Shi, H. Zhou, *Chem. Commun.*, 2014, **50**, 1215.

45 Y. X. Wang, S. L. Chou, H. K. Liu, S. X. Dou, *Carbon*, 2013, **57**, 202.

TOC

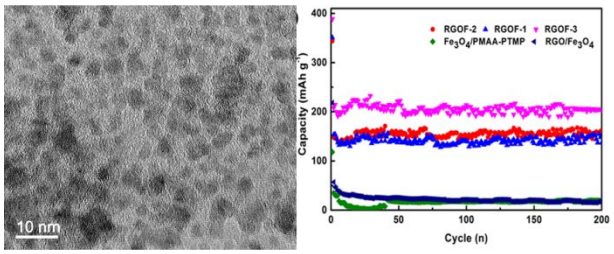

Nanocomposites with ultra-small Fe_3O_4 nanoparticles uniformly anchored on reduced graphene oxide nanosheets have been synthesized as excellent anodes for sodium-ion batteries.